


A high-speed variable-temperature ultrahigh vacuum scanning tunneling microscope with spiral scan capabilities F

Cite as: Rev. Sci. Instrum. **93**, 053704 (2022); <https://doi.org/10.1063/5.0079868>

Submitted: 25 November 2021 • Accepted: 08 April 2022 • Published Online: 11 May 2022

 Zechao Yang,  Leonard Gura,  Florian Kalaß, et al.

COLLECTIONS

 This paper was selected as Featured



View Online



Export Citation



CrossMark

ARTICLES YOU MAY BE INTERESTED IN

[Ultra-high vacuum cleaver for the preparation of ionic crystal surfaces](#)



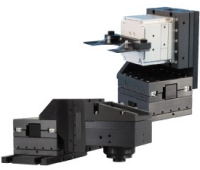
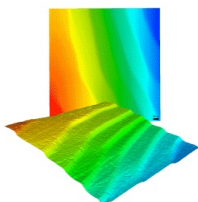
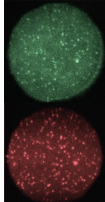
Review of Scientific Instruments **93**, 053703 (2022); <https://doi.org/10.1063/5.0088802>

[Shot-noise measurements of single-atom junctions using a scanning tunneling microscope](#)

Review of Scientific Instruments **93**, 023702 (2022); <https://doi.org/10.1063/5.0078917>

[A qPlus-based scanning probe microscope compatible with optical measurements](#)

Review of Scientific Instruments **93**, 043701 (2022); <https://doi.org/10.1063/5.0082369>

 MCL MAD CITY LABS INC. www.madcitylabs.com	<p>Nanopositioning Systems</p> 	<p>Modular Motion Control</p> 	<p>AFM and NSOM Instruments</p> 	<p>Single Molecule Microscopes</p> 
---	--	--	---	--

A high-speed variable-temperature ultrahigh vacuum scanning tunneling microscope with spiral scan capabilities

Cite as: Rev. Sci. Instrum. 93, 053704 (2022); doi: 10.1063/5.0079868

Submitted: 25 November 2021 • Accepted: 8 April 2022 •

Published Online: 11 May 2022



View Online



Export Citation



CrossMark

Zechao Yang,  Leonard Gura,  Florian Kalaß,  Patrik Marschalik, Matthias Brinker, William Kirstaedter, Jens Hartmann, Gero Thielsch, Heinz Junkes,  Markus Heyde, ^{a)}  and Hans-Joachim Freund 

AFFILIATIONS

Fritz-Haber-Institut der Max-Planck-Gesellschaft, Faradayweg 4-6, 14195 Berlin, Germany

^{a)} Author to whom correspondence should be addressed: heyde@fhi-berlin.mpg.de

ABSTRACT

We present the design and development of a variable-temperature high-speed scanning tunneling microscope (STM). The setup consists of a two-chamber ultra-high vacuum system, including a preparation and a main chamber. The preparation chamber is equipped with standard preparation tools for sample cleaning and film growth. The main chamber hosts the STM that is located within a continuous flow cryostat for counter-cooling during high-temperature measurements. The microscope body is compact, rigid, and highly symmetric to ensure vibrational stability and low thermal drift. We designed a hybrid scanner made of two independent tube piezos for slow and fast scanning, respectively. A commercial STM controller is used for slow scanning, while a high-speed Versa Module Eurocard bus system controls fast scanning. Here, we implement non-conventional spiral geometries for high-speed scanning, which consist of smooth sine and cosine signals created by an arbitrary waveform generator. The tip scans in a quasi-constant height mode, where the logarithm of the tunneling current signal can be regarded as roughly proportional to the surface topography. Scan control and data acquisition have been programmed in the experimental physics and industrial control system framework. With the spiral scans, we atomically resolved diffusion processes of oxygen atoms on the Ru(0001) surface and achieved a time resolution of 8.3 ms per frame at different temperatures. Variable-temperature measurements reveal an influence of the temperature on the oxygen diffusion rate.

© 2022 Author(s). All article content, except where otherwise noted, is licensed under a Creative Commons Attribution (CC BY) license (<http://creativecommons.org/licenses/by/4.0/>). <https://doi.org/10.1063/5.0079868>

I. INTRODUCTION

Since its invention by Binnig and Rohrer in 1982, the scanning tunneling microscope (STM) has become one of the most powerful instruments for real-space investigation of surfaces at atomic resolution.¹ This technique has broad capabilities, with sample systems ranging from metal crystals to thin insulating films and from quantum materials to biological membranes, combined with the possibility to vary the measuring conditions from mK to several hundred degree Celsius from high pressure to ultra-high vacuum (UHV) environment.²⁻⁵ However, an improved time resolution in STM is often missing for further applications. Inspired by pump-probe techniques,⁶ time resolutions ranging from nanoseconds to subpicoseconds have been achieved in STM measurements by incorporating voltage, laser, or terahertz pulses into the tunneling junction.⁷⁻¹¹ Such experiments have enabled studies on dynamics of

spins, charge carriers, and quasiparticles upon excitation in nanostructures. Moreover, the spectroscopy mode of STM allows us to investigate the vibrational and rotational properties of molecules through inelastic electron tunneling spectroscopy (IETS)¹²⁻¹⁴ at the femtosecond scale. Unfortunately, these concepts do not allow for imaging in real space at such time resolutions. To directly access the non-equilibrium dynamics of atom diffusion,^{15,16} film growth,¹⁷⁻¹⁹ phase transitions, and chemical reactions,²⁰⁻²³ much effort has been made to drive the imaging rates of STM close to the video rate and beyond in the last two decades. [Figure 1](#) depicts the application and limitation of different techniques for resolving dynamic processes, and [Table I](#) summarizes the time resolutions of state-of-the-art high-speed STMs for real-time imaging.

One bottleneck for fast scanning is the mechanical stability of the scanner unit. In order to avoid any interference between the

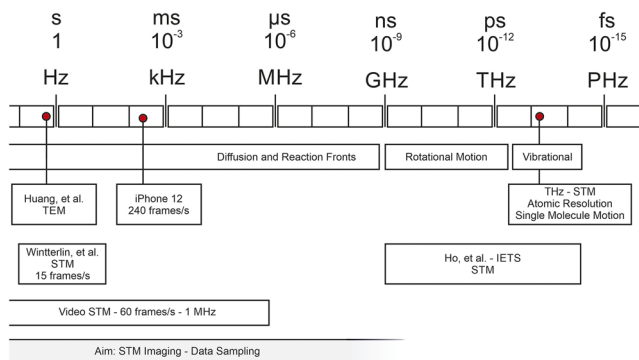


FIG. 1. Overview of the time scale of molecular and atomic dynamic processes and the time resolution of different techniques.

piezo-movement and the mechanical response of the system, it is crucial to push the resonance frequency of the scanner above the desired scan speeds. To increase the bandwidth of the mechanical loop, it is necessary to build the STM head as rigid and compact as possible. Several groups have contributed to the development of stable mechanical loops with a high resonance frequency to increase the imaging rate.^{24,27,29–36} Their methods include using stiff coarse approach mechanisms, such as inchworm motor or Pan style motor, design of scanners with different configurations ranging from tube piezo shape to conical piezo geometry and further to microelectromechanical systems (MEMS) scanners and flexure-based scanners, and so on.³³

Another challenge is driving the scanner piezo with a frequency of several hundreds of kilo Hertz in order to achieve scans at the video rate. Conventionally, the STM tip scans in raster geometry controlled by triangle waveforms. To avoid the high frequency components associated with the turn-around points, sine waves have been employed to control the movement along the fast scan direction.^{15,26–28,31,34,35,37} However, distortions and imaging artifacts could not be completely eliminated at the edge of the STM images, particularly at high speed.^{25,27,33,38} Applying smooth sine waves in both scan directions should further minimize imaging artifacts and improve the time resolution. Spiral geometries represent a promising possibility to implement these smooth sine waves. With spiral geometries, the tip scans all the points smoothly minimizing the

effects of hysteresis and creeping of the piezo. Moreover, by moving in both x and y directions synchronously, theoretically the spiral geometry achieves the maximum scan rate and area with a certain resonance frequency and scan voltage. Recently, the spiral scan has been used in atomic force microscopy and electron microscopy to improve the imaging quality^{39–45} and also in STM to correct the image distortions.^{46,47} However, so far the effect of spiral scans on increasing the frame rate in STM imaging has not been explored.

In addition, there are some other factors determining the scan speed and image resolution of the high-speed STM. A high bandwidth of the feedback control system is required to track the tip-sample distance during high-speed scanning in a constant current mode. In fact, the constant height mode is usually used to compromise between the high-speed scan and the rather slow feedback loop limited by the stray capacitance.^{15,26,28} In parallel, a higher bandwidth of the preamplifier for detecting the tunneling current is helpful to improve the imaging resolution. Strong oversampling is crucial to recover useful signals when scanning above the preamplifier cut-off frequency. Further developments in high-speed electronics will naturally provide new solutions for data acquisition and visualization for high-speed STM imaging. Table II shows a summary of the bandwidths of state-of-the-art commercially available high-speed electronics that limit the high-speed imaging in STM.

In addition to high-speed imaging, the ability to vary the sample temperature enables STM to be a versatile tool that allows us to determine the kinetic parameters for the surface dynamics. Scanning at high temperatures favors thermal drift in the system and potentially causes image distortions. To reduce image distortions due to thermal drift, the shape of our scanner is cylindrically symmetric.^{31,52} Moreover, the scanner made of piezos must be kept at a temperature lower than their Curie temperatures during high temperature measurements. One method is thermally isolating the scanner from the hot sample with radiation shields.^{31,52} A more efficient way is counter-cooling the entire microscope body with a cryostat.³² Table III summarizes the scanning parameters of state-of-the-art high-temperature STMs.

In this article, we present the design and performance of a variable-temperature high-speed scanning tunneling microscope working in the UHV environment. We developed a sample holder with an integrated e-beam heater that enables *in situ* heating during STM imaging. On the other hand, the whole STM is located within a continuous flow cryostat for counter-cooling the scanner during high-temperature measurements. The microscope body is compact,

TABLE I. Scanning parameters of state-of-the-art high-speed STMs.

Environment	Sample system	Image size (nm ²)	Resolution	Imaging speed (Hz)	Reference
RT-UHV	O diffusion on Ru(0001)	8 × 8	Atomic	15	15
Liquid	S diffusion on Cu(100)	9.4 × 9.4	Atomic	20	24
Ambient	HOPG	1 × 1	Atomic	52	25
LT-UHV	Molecular self-assembly	6 × 6	Submolecular	60	26
HT-UHV	Graphene growth on Ni(111)	1.5 × 3	Atomic	60	19
RT-UHV	HOPG	5 × 5	Atomic	80	27
HT-UHV	Surface reconstruction of Rh(110)	6.5 × 6.5	Atomic row	100	28

TABLE II. Bandwidths of state-of-the-art high-speed electronics compared with the electron tunneling limit.

Electronics	Bandwidth (Hz)	Bandwidth (s)	Reference
Electron tunneling	3 G (1 nA)	0.33 n	34
Real-time controller	30 k	33 μ	48
Preamplifier	600 k (10 ⁹ V/A)	1.7 μ	49
Digitizer	500 M	2 n	50
HV amplifier	5 M	200 n	51

TABLE III. Scanning parameters of state-of-the-art high-temperature STMs.

Sample system	Temperature (K)	Reference
Surface reconstruction of Rh(110)	473	28
Fischer-Tropsch synthesis on Co(0001)	500	53
Graphene growth on Ni(111)	710	19
Phase transition on Si(111)	930	54
Boron nitride growth on Rh(111)	978	17

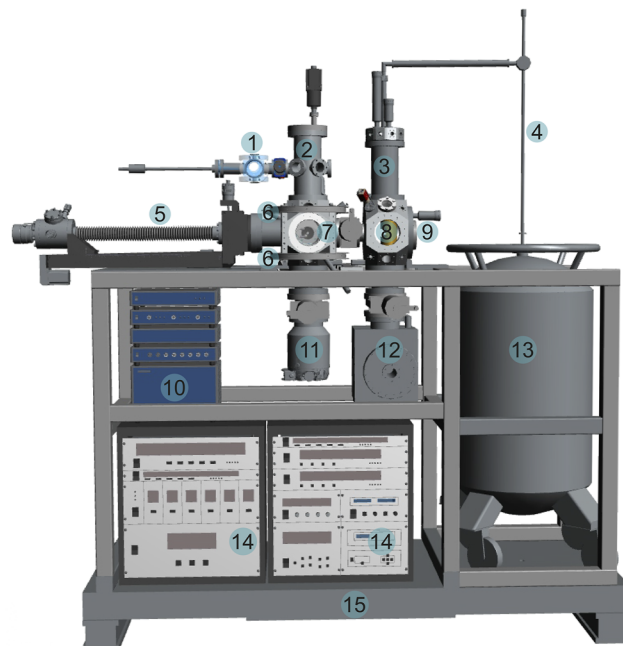
rigid, and damped by suspension springs and eddy current, which result in high vibrational stability. We use spiral scan geometries for the high-speed imaging of atomically flat surfaces. High-speed scans are controlled by a custom-programmed high-speed Versa Module Eurocard bus (VMEbus) system. During fast scanning, the feedback on the tunneling current is still switched on but set to a very slow feedback loop. This allows us to control an average tunneling current. Hereby, the tip scans in a quasi-constant height mode. Oxygen adsorption on Ru(0001) is measured for testing the performance of the instrument. A scan speed of 120 frames per second with atomic resolution is achieved at room temperature and elevated temperatures. The diffusion processes of single oxygen atoms can be observed in the recorded STM videos.

II. DESIGN AND CONSTRUCTION

In order to achieve atomic resolution in the high-speed STM imaging above the video rate, both the mechanical and electronic noise levels must be reduced as much as possible. The sample holder with an *in situ* heating function and an easy sample transfer system in the UHV environment is home-designed. To limit the mechanical noise, we constructed an STM scanner that is compact and rigid and fairly insusceptible to external vibrations. To efficiently increase the frame rate, we implemented spiral geometries for fast scanning. The details of the constructions will be described below.

A. System overview

The machine is a two-chamber system, including a main chamber and a preparation chamber, as shown in Fig. 2. The preparation chamber is equipped with standard preparation tools for sample cleaning and thin film growth, such as sputter gun, e-beam evaporator, and residual gas analyzer. The top of the preparation chamber is attached with a sample storage for hosting up to eight sample holders in UHV, which is connected to the load lock from the side. In

**FIG. 2.** Overview of the vacuum system including the flow cryostat. The whole setup is fixed on a vibration isolating table to damp the mechanical noise during measurement: (1) load lock, (2) sample storage, (3) cryostat flange, (4) liquid helium or nitrogen transfer tube, (5) manipulator, (6) Helmholtz coil for IV-LEED, (7) preparation chamber, (8) STM body, (9) main chamber, (10) Nanonis control system, (11) turbo pump, (12) ion pump, (13) liquid helium or nitrogen can, (14) electronics, and (15) vibration damping table.

addition, an ErLEED (SPECS Surface Nano Analysis GmbH) resides in the preparation chamber for characterizing the overall surface structure of single crystals and adsorbate layers upon sample preparation. The main chamber that is connected with the preparation chamber through a gate valve hosts a continuous flow cryostat. The microscope is housed in the bottom part of the cryostat under UHV and low temperature environment. The preparation chamber and the main chamber are connected from the bottom to a turbomolecular pump and an ion getter pump, respectively. This combination assures a base pressure in the 10⁻¹⁰ mbar range for both chambers.

For mechanical stability, the chambers are mounted on a rigid steel frame. Additionally, the complete system, including the liquid helium, rests on an Opta optical breadboard supported by three vibration damping legs from HWL Scientific Instruments GmbH. To minimize the external vibrations due to cable connections, electronic controllers are also placed in the frame. Moreover, the high-speed digitizer and high voltage amplifiers with cooling fans are located on an additional frame close to the main chamber. Therefore, during STM measurement, the entire system is well isolated with only several short cables connected from the external environment.

B. Sample holder design

The surface dynamic processes are strongly influenced by the sample temperature. In particular, kinetic parameters, such as

activation energy, can be extracted by means of the Arrhenius equation in the temperature-dependent experiments. To this end, we designed a sample holder with a built-in electron bombardment heater, which can be used for annealing the sample during sample preparation and heating the sample in STM during imaging. The built-in heater also allows for *in situ* investigating the overall structural evolution of the films on surfaces as a function of temperature with LEED.

Figure 3 sketches the structure of the sample holder that consists of several stacked layers. A metal ring with threads and a metal base with screws are located at the most top and most bottom positions, respectively. They are made from molybdenum and used to hold all the other components in between. Three sapphire plates are placed in between the metal units from top to down to create two isolating layers. The sample is placed in between the top and the middle sapphires, connected with K-type thermal couples for measuring the sample temperature. The filament made from tungsten and its electrodes made from molybdenum are inserted in between the middle and the bottom sapphires. With this setup, it is assured that both the sample and the filament are electrically isolated from their environments. For electron bombardment heating, the sample is grounded and a current is applied to the filament with a lower potential with respect to the sample for emitting hot electrons to the sample.

This design of the sample holder ensures fast and easy sample transfer, as shown in Fig. 4. The sample holder is in an overall rectangular shape with a nose at the molybdenum base that can be grabbed by the manipulator head. Electrical connections are made between the pins at the sample holder and those at the manipulator for filament current and temperature measurement. An electrically insulating spacer made from Macor is incorporated in between the manipulator metal body and its head, which enables the sample holder to be electrically decoupled from the ground.

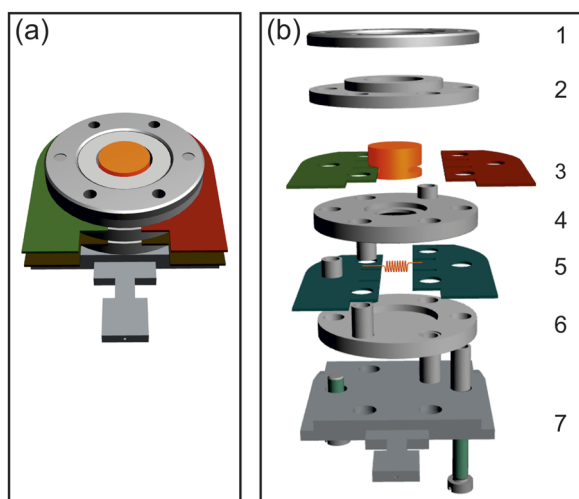


FIG. 3. Design of the sample holder with a built-in e-beam heater. (a) Overview of the sample holder showing an overall rectangular shape with a nose for sample transfer. (b) Structure of the sample holder: (1) Mo ring with threads, (2) top sapphire, (3) single crystal and thermal couple plates, (4) middle sapphire, (5) W filament and its electrodes, (6) bottom sapphire, and (7) Mo base with screws.

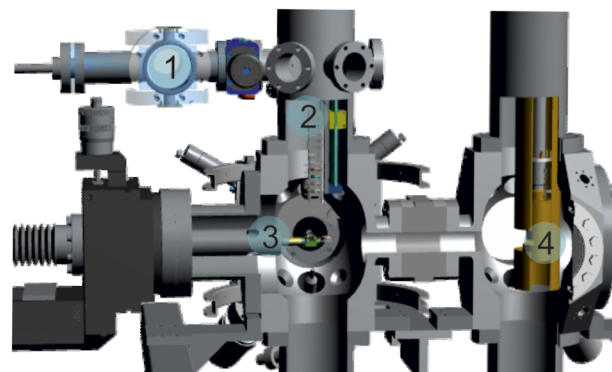


FIG. 4. Sample transfer system. A sample can be introduced into the UHV system from ambient through the load lock (1). Then, the sample can be transferred to the sample storage position (2), where up to eight samples can be stored. The manipulator (3) can be used to grab a sample from the sample storage for film preparation. In the end, the sample is transferred into the STM (4) for measurement.

C. Continuous flow cryostat

Since the sample needs to be heated in the STM during temperature-dependent measurements, it is necessary to counter-cool the scanner unit to minimize the thermal drift and keep the piezos under their Curie temperature. Moreover, the spectroscopy mode of the microscope can offer another interesting possibility to investigate the local vibrational properties of the nanostructures on surfaces through IETS,¹² whose prerequisite is a low temperature environment. For these purposes, a continuous flow cryostat is chosen for cooling the STM.⁵⁵

Figure 5 shows the flow cryostat that is designed by ourselves and built by the CryoVac GmbH. Liquid nitrogen or liquid helium is led into the inlet, while the outlet is connected to the exhaust line. A typical pressure of several hundreds of mbar is achieved in the exhaust line by a membrane pump, which facilitates the continuous flow of liquid nitrogen or liquid helium through the cryostat. The STM head is located inside the cryostat enclosed by two layers of radiation shields, which thermally decouple the STM from the room temperature environment and enable effective cooling of the whole microscope and not only the sample. Sample transfer can be realized by opening a shutter thermally connecting to the radiation shields by thick copper braids. The microscope is mechanically attached to the cryostat cold finger with a locking mechanism. Thereby, the microscope can be firmly attached to the cryostat for fast cooling as well as for rigidity during sample transfer. Upon releasing, the microscope is held by three springs from the cryostat for damping the mechanical vibrations during measurement.

D. STM head

1. Design of the microscope

Figure 6 shows the home-built STM head suitable for high-speed scanning at variable temperatures. It has been designed to be as compact and rigid as possible so that it is less sensitive to external vibrations. Additionally, the microscope has an overall cylindrical shape with an exact mirror symmetry along the probe axis [Fig. 6(a)]. This assures the alignment of the probing tip relative to the sample

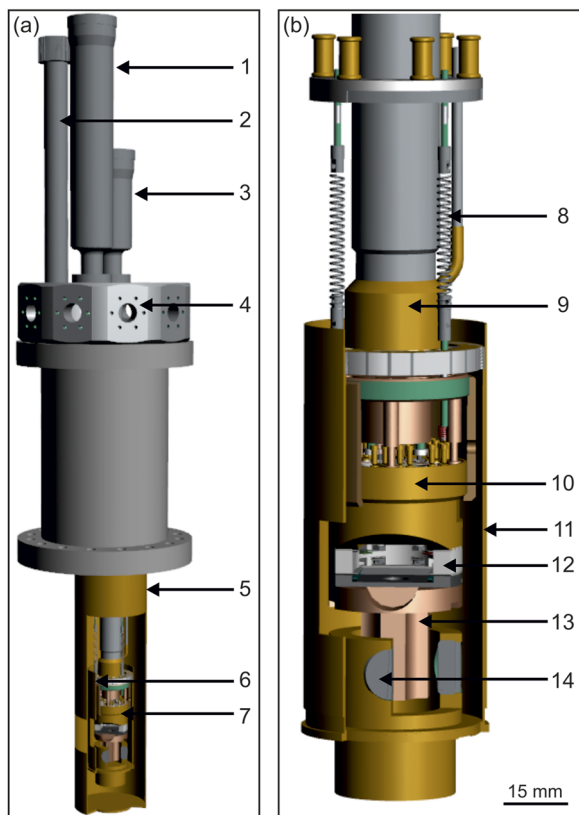


FIG. 5. (a) Design of the flow cryostat: (1) shutter controller, (2) liquid inlet, (3) clamp controller, (4) ports for electrical feedthroughs, (5) outer shield, (6) inner shield, and (7) microscope. (b) Sectional view of the microscope mounted within the cryostat: (8) springs, (9) cold finger, (10) microscope body, (11) inner shield, (12) sample holder, (13) copper cross, and (14) magnets. During measurement, the microscope is unclamped from the cold finger of the cryostat and hanging on three springs. At the bottom of the sample stage, an eddy current damping system is used to further reduce the vibration noise. For better visibility of the microscope, the front shields are removed.

during temperature changes. The compactness is realized primarily by integration of the tube scanner into the coarse approach motor [Fig. 6(b)]. It consists of a copper cylinder (walker) carrying the scanner, which is clamped between three shear-piezo stacks glued at a copper block. We drive the motor in the stick-slip mode of operation. Each shear piezo can enable independent displacements in two directions, which can be named as x and z directions for easy description. The coarse approach is realized by simultaneous displacements of the three shear piezos in the z direction. Similarly, the simultaneous displacements in the x direction capacitate the rotation of the scanner. We incorporated six slits at the copper walker. This enables elasticity to the walker so that the friction force within the coarse approach system is stable during the stick-slip motion. Since all the metal parts are made of the same material, gold-coated copper, the coarse motor is very stable and reliable at variable temperatures. Instead of the commonly used prismatic shape, we use a cylindrical shape and placed the tip off center. This enables coarse changes of the scan position by rotating the scanner.

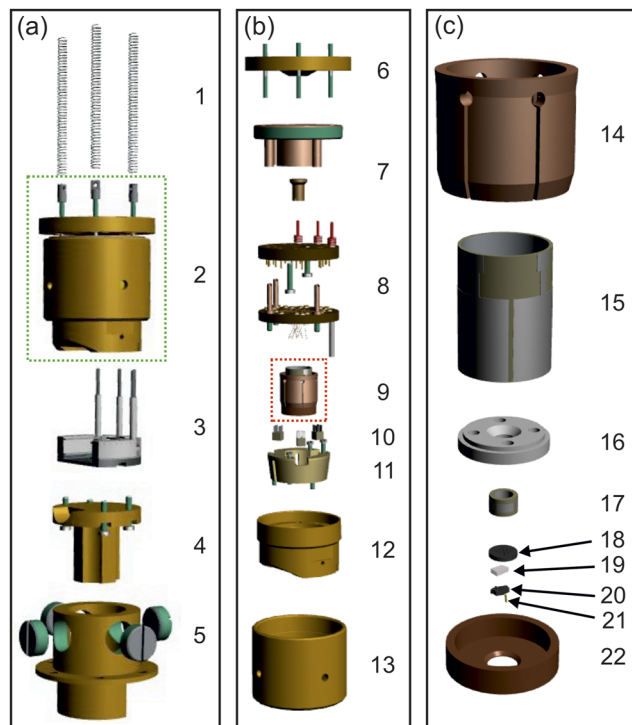


FIG. 6. (a) Schematic of the STM head: (1) springs, (2) microscope, (3) sample stage, (4) copper cross of eddy current damping, and (5) magnets of eddy current damping. The microscope is hanging on three springs from above and connects to an eddy current damping setup from underneath, which ensure highly vibrational stability during measurement. (b) Design of the microscope [the part highlighted in the dashed green rectangle in (a)]: (6) connection to cryostat, (7) parts for clamping, (8) electrical connections, (9) scanner unit, (10) shear piezos for the coarse approach, (11) copper block, and (12) and (13) microscope body. The coarse approach is realized through the stick-slip mechanism. (c) Design of the scanner unit [the part highlighted in the dashed red rectangle in (b)]: (14) copper walker, (15) overview piezo, (16) Macor connector, (17) fast-scan piezo, (18) graphite, (19) insulation spacer, (20) tip holder made from graphite, (21) tip, and (22) copper shield. The hybrid scanner consists of two independent tube piezos. The cuttings allow for elasticity to the copper walker, ensuring stability of the coarse approach at variable temperatures.

As shown in Fig. 6(b), two brackets with plugs and sockets are designed for the electronic connections. The plugs are fed into the electronics out of the UHV through the cryostat, while the sockets are connected to the cables from the scanner and shear piezo stacks. The bracket with the sockets can be easily disconnected from the bracket with the plugs that are fixed onto the cryostat, thereby keeping the repair of the scanner simple. Moreover, the same electrical contacts as those at the manipulator are also designed at the sample stage for *in situ* e-beam heating and temperature monitoring during scanning. A copper cross is attached at the bottom of the sample stage, together with four strong magnets mounted from underneath, to construct an eddy current damping system [Fig. 6(a)].

2. Hybrid scanner

The scanner unit is the heart of the STM head. In our setup, we designed a nested hybrid scanner composed of two

independent segmented tube piezos [Fig. 6(c)], a big one and a small one in dimension, from Physik Instrumente GmbH (PI). The big piezo is used for large-area and low-speed scans, named as overview (OV) piezo. Once a good place has been found, one can start the fast scan in a small area by using the small piezo named as fast-scan (FS) piezo. In the hybrid scanner, the two piezos are independently controlled by two sets of electronics (see details in Sec. II E 2). Therefore, there is no need to frequently switch the control electronics between slow and fast modes, and it is convenient to change the fast scanning position during the measurement by adjusting the voltages applied at the OV piezo.

The maximum scan range with an applied voltage of ± 200 V amounts to $2500.0 \times 2500.0 \text{ nm}^2$ for the OV piezo and $500.0 \times 500.0 \text{ nm}^2$ for the FS piezo at room temperature.

A critical parameter for the piezo scanner is its resonance frequency, which should be higher than the scanning frequency in the fast scan direction. Otherwise, the scanning motion would excite mechanical noise in the piezo. Here, we chose a FS piezo with resonance frequencies above 1 MHz that is well above the scheduled scan speed.

Figure 6(c) shows the assembly of the hybrid scanner. The top part of the OV tube piezo is mounted into the copper cylinder without establishing an electric connection. The FS piezo is attached onto the bottom of the OV piezo through a Macor connector. Here, it is important to note that the four segments on the outer face at the FS piezo must be aligned to those at the OV piezo to ensure the same tilt angles in the x and y directions for both tube piezos. Then, three stacks (a graphite piece, an insulation spacer made of sapphire, and another graphite piece with holes as the tip holder) are glued onto the bottom of the FS piezo. The tip is clamped off center of the graphite support to coarsely change the scan area by rotation of the scanner. The graphite between the FS piezo and the tip is set to the ground potential, which is essential to reduce the electronic noise in the tunneling current. Graphite is used due to its low density to ensure a high resonance frequency of the FS piezo for high-speed measurements. A copper shield is fixed onto the bottom of the copper cylinder with conductive glue. This shield is also set to ground potential, which is used to shield the high frequency signals at the FS piezo to avoid cross talk with the tunneling current signal during fast scan.

Figure 7 depicts the sectional view of the assembled microscope. It measures 35 mm in diameter by 60 mm in height, including the copper cross for eddy current damping. There are in total 12 cables for the hybrid scanner: two sets of five cables for piezo electrodes (four segments on the outer face, one on the inner), one cable for the tunneling current, and one cable for grounding the copper shield. Here, we chose copper instead of the often used nickel to avoid magnetic material. The cables for the piezo electrodes are feed into the pins through the tube, while the tunneling current cable passes through the microscope body to avoid cross talk.

E. Spiral scanning and electronics

1. Spiral scanning

To overcome the limitation of scan speed by the sharp turn-around points in the conventional raster scanning mode, we implement spiral geometries for the high-speed scans in our

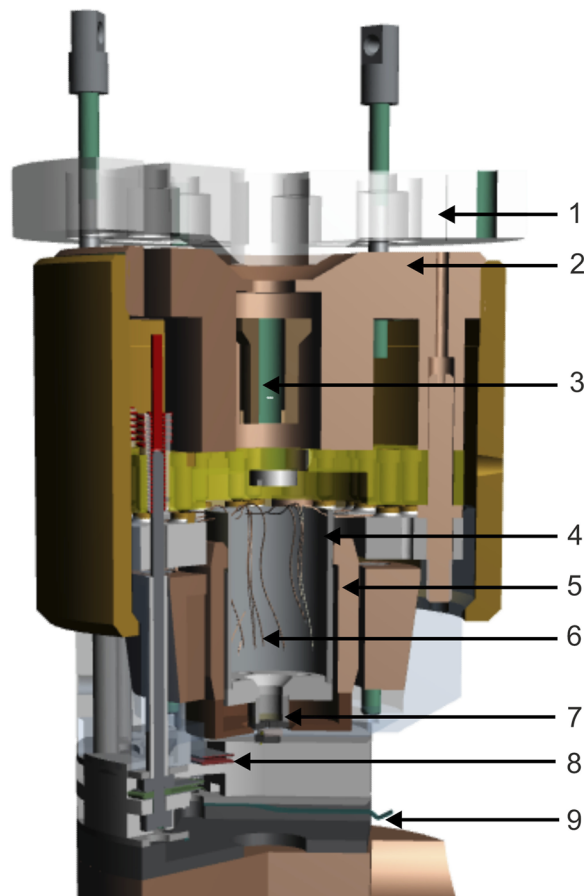


FIG. 7. Sectional view of the assembled microscope: (1) connection to the cryostat, (2) contact parts of the microscope, (3) central rod to clamp and release the microscope, (4) overview piezo, (5) copper walker, (6) cables, (7) fast-scan piezo, (8) electrical connections at sample holder, and (9) springs for fixing the sample holder.

experiments.^{39–45,56,57} In spiral scanning, the signals are generated by smooth variation of the output frequency and amplitude in real time.

Mathematically, a spiral can be described as the combination of cosine and sine waves,

$$x = t^a \cdot \cos(\omega \cdot t^b), \quad (1)$$

$$y = t^a \cdot \sin(\omega \cdot t^b). \quad (2)$$

The spiral trajectory can be adjusted by parameters a and b . For example, $a = b = 1$ leads to spiral scanning with constant angular velocity (CAV), while spiral scanning with constant linear velocity (CLV) can be generated by $a = b = 0.5$. The waveforms for control of a spiral scan in constant angular velocity are shown in Fig. 8(a). The input signals for x and y directions show a phase shift of 90° , and the amplitude of the signals varies linearly with time. The corresponding trajectory of the tip during scanning is depicted in Fig. 8(b), which clearly illustrates that in the CAV mode, more data points

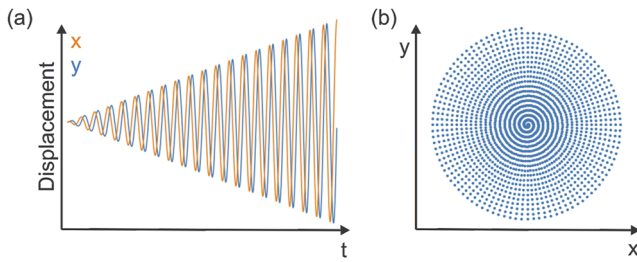


FIG. 8. (a) Waveforms for control of a spiral scan in constant angular velocity. (b) The corresponding trajectory of the tip for a scan with constant sampling frequency. The sample density is reduced for visualization.

are distributed in the central area. Although in the CLV mode the data points are evenly distributed in the whole scan area, the very fast motion of the tip in the center will induce pronounced vibrational noise and influence the resolution in the STM images.⁴⁵ The CAV spiral scanning in our measurements has turned out to be more stable (less noise) than the CLV spiral mode.⁵⁷

When scanning with high speed, it is crucial to apply tilt correction to the spiral geometry to avoid tip crashes with the surface [Fig. 9(a)]. In our method, we integrated a common offset z into the x and y signals since the inner electrode of the FS piezo is grounded in our scanner. With the tilt correction, the waveform is described as

$$x' = t \cos(\omega t) + z, \quad (3)$$

$$y' = t \sin(\omega t) + z. \quad (4)$$

The z signal is a linear combination of x and y ,

$$z = Ax + By. \quad (5)$$

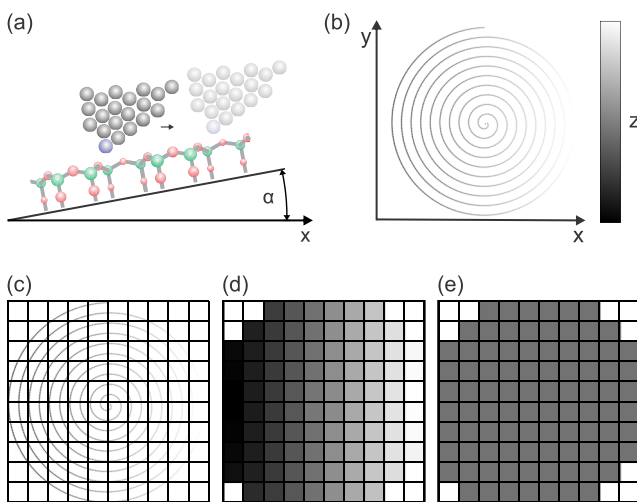


FIG. 9. (a) Schematic of the tilt correction. (b) Planar tilt correction applied to the STM tip trajectory to scan in the quasi-constant height mode. (c) Spiral trajectory of the tip movement from (b) with an overlaid 2D grid. (d) 2D histogram of set tilt correction in the z direction and (e) the resulting ideal tunneling current.

Here, A and B represent the tilt angles in x and y directions, respectively, which can be extracted from the OV piezo during conventional raster scan. With simple trigonometry, the prefactors A and B can be determined as

$$A = -\tan(\alpha + \alpha_{\text{offset}}) \cdot f_{\text{OV}}/f_{\text{FS}}. \quad (6)$$

Here, α is the tilt angle in x direction measured with the OV piezo and α_{offset} is the angle misalignment of the OV piezo respect to the FS piezo in x direction. f_{OV} and f_{FS} are the calibration factors (nm/V) for the OV piezo and the FS piezo, respectively,

$$B = -\tan(\beta + \beta_{\text{offset}}) \cdot f_{\text{OV}}/f_{\text{FS}}. \quad (7)$$

Here, β is the tilt angle in y direction measured with the OV piezo and β_{offset} is the angle misalignment of the OV piezo respect to the FS piezo in the y direction. Figure 9(b) illustrates the intensity profile of a spiral trajectory with the tilt correction in x direction, where the brightness represents the height. The exemplarily shown correction consists of a simple planar tilt. In principle, other functions are implementable to correct for non-atomically flat surfaces.

Besides the tilt correction, another key factor to enable fast scanning and to avoid tip crashes is the smooth transition between outward and inward scans by the constant direction of rotation along the spiral trajectory.⁵⁷ The tip starts in the center with the outward scan in a clockwise motion. At the end of the spiral trajectory, the tip continues immediately with the inward scan in clockwise motion too. Therefore, the overall trajectory is continuous and does not show abrupt changes in direction. Moreover, we implemented a method to stop high-speed scanning slowly by steadily decreasing the amplitude of the spiral input signals over several outward and inward scans until the tip is at the zero reset position.

To display the spiral data as an image, we need to map the data cloud onto a two dimensional (2D) grid. Figures 9(c) and 9(d) sketch a fast method to achieve this with 2D histograms. Figure 9(c) shows how the spiral point cloud is binned by the 2D grid. In Fig. 9(d), the set tilt correction in the z direction is plotted, and in Fig. 9(e), the resulting tunneling current is shown. Here, each square (pixel) is assigned with the mean intensity value of all spiral points inside this area. With this method, we are able to provide a live monitor during the fast scanning. The calculation time for a 100×100 grid image takes 3.5 ms. With an additional plane removal of the data, the calculation time increases to not more than 10 ms per frame. To analyze the spiral images in detail, a purely Python based program is developed.^{57,58} Details on other possible image reconstructions are described elsewhere.⁵⁷

2. Electronics

The hybrid scanner is controlled with a hybrid electronics system by the combination of a commercial SPM control unit and a home-programmed high-speed electronics (Fig. 10). The Nanonis control system from SPECS Surface Nano Analysis GmbH is used for the OV scanner in the conventional scanning (low-speed and large-area measurements). For the video-rate scanning, we choose a high-speed Versa Module Eurocard bus (VMEbus) system to control the FS scanner and process the data. During fast scanning, the tunneling current signal is fed into both the Nanonis unit and the high-speed electronics. When the FS piezo scans in high-speed

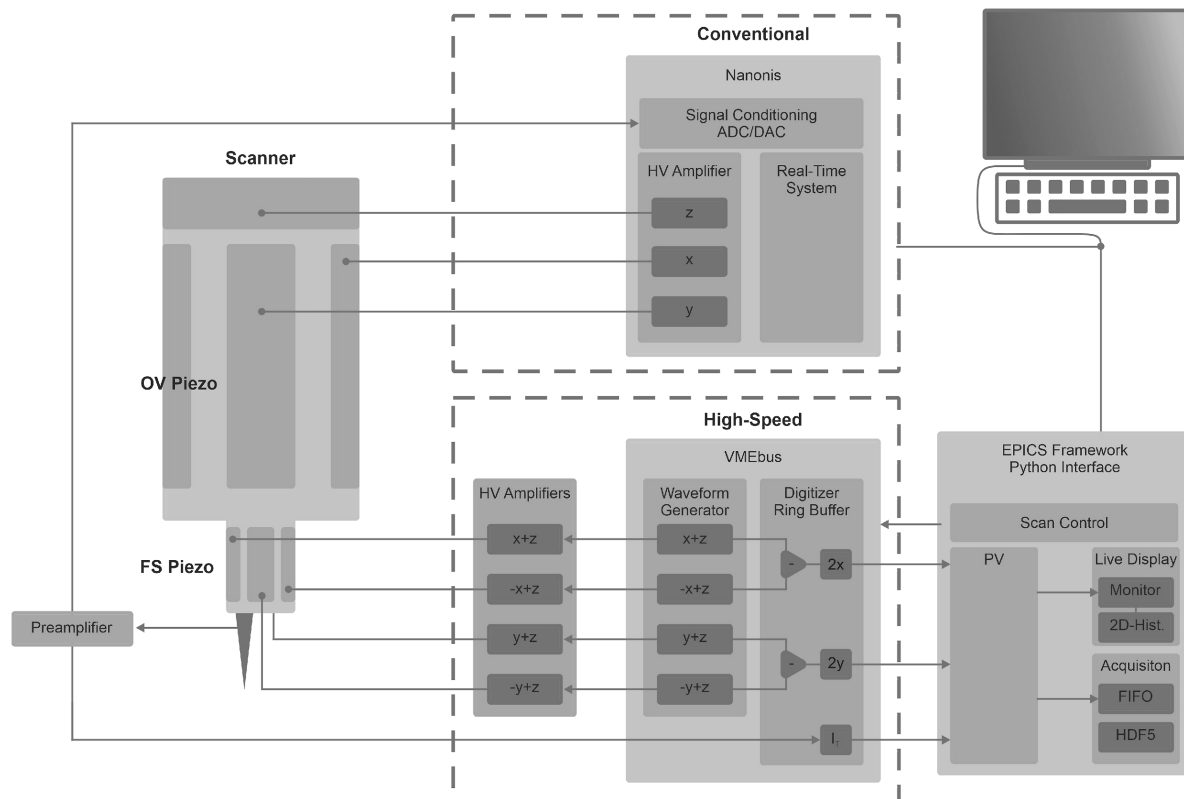


FIG. 10. Schematic view of the electronics for controlling the hybrid STM scanner. A commercial Nanonis unit and a high-speed Versa Module Eurocard bus system control the OV and the FS piezo for slow and fast scan, respectively. Fast scan control and data acquisition have been programmed in an EPICS framework.

spiral geometry, the feedback of the OV piezo is still switched on through the Nanonis unit but set to a very slow feedback loop with typical parameters of 5 pm for proportional and 100 ms for time constant. Therefore, the tip scans in a quasi-constant height mode, where the logarithm of the tunneling current signal can be regarded as roughly proportional to the surface topography. It is worthy to note that the cut-off frequency of the Nanonis real-time system is 30 KHz that is well below the bandwidth of the tunneling current signal in high-speed scanning. Hence, it acts as a low-pass filter to remove the high frequency noises activated by the tip motion, thereby avoiding overshooting in the feedback system during fast scanning.

The high-speed electronics consists of four high voltage amplifiers and a VMEbus system, including a waveform generator and a digitizer.⁴⁶ The arbitrary waveform generator (with an output range of 3 V peak to peak) is used to produce the sine and cosine waves for the spiral scans. Subsequently, the signals are routed into the high voltage amplifiers that allow ± 150 V output range and up to 5 MHz bandwidth through digital-to-analog converters (DACs). There are four signals applied to the four segments on the outer face of the FS piezo, while the inner electrode is grounded. Moreover, an additional z signal is added to the four outer segments (for example, the z in the “x + z” signal) to elongate or shorten the entire tube piezo

simultaneously; hence, the tilt correction can be applied during high-speed scanning. This z signal can be calculated from the tilt angles in x and y directions measured from Nanonis (see Sec. II E 1). The tilt correction is critical for high-speed STM images resulting in tip crashes. The slow feedback from Nanonis only compensates the drift of the mean vertical tip position. Actually, during measurement, the height signal of the OV piezo is also fed into the data acquisition system of the high-speed electronics for analyzing the quality of the tilt correction and the reliability of the features in the STM images.

The high-speed digitizer is used to digitize the tunneling current signal from the preamplifier. While the typical bandwidth required for video-rate STM measurements stays in the MHz frequency range, commercially available preamplifiers provide a rather smaller bandwidth, thus resulting in a strong suppression of the signals in the frequency range of interest. In this context, the high sampling rate with 250 MS/s of the SIS3316 VME digitizer allows oversampling the input to recover the measured signal even well above the preamplifier cutoff. For the first test, we use a FEMTO DLPCA200 I/V converter with a cut-off frequency (-3 dB) of 200 KHz with the gain setting 10^8 V/A. The digitizer is driven by the same clock as the waveform generator, thereby ensuring stable and reliable synchronization between the probe motion and the data acquisition.

A high-efficiency integrated software suite is needed to account for real time processing and storing of the data acquired with the high-speed electronics. As an example, the stream of data during the acquisition of a 200×200 pixels movie at an imaging rate of 50 frames per seconds with a resolution of 14 bit amounts to 28 Mbit/s. We choose the experimental physics and industrial control system (EPICS) framework to drive the control electronics. Phoebus is used as the graphical user interface to monitor the process variables (PV) to configure the scan parameters and to visualize the high-speed scan results during the data acquisition. We acquire the position (x, y, z) and the tunneling current signals with the SIS3316 VME digitizer. The data are stored in a ring buffer on an additional local central processing unit (CPU). From here, the data are written to a PV in the EPICS framework. With a monitor function of the pvapy⁵⁹ package, we collect each frame and append it to a queue on our local machine. Another thread in Python accesses the queue and writes the single frames into an HDF5 file. The frames are provided with numerous attributes, such as frame numbers, gains, and real-time timestamps. For the live scan display, an independent process collects single frames and maps the data to a 2D histogram (as describes in Sec. II E 1). An additional PV provides the output image, which is then displayed in Phoebus on the local measurement machine.

III. PERFORMANCE

The principal tests of our facility concern the image quality of the conventional scanning, the lateral resolution, and speed limit in the fast spiral scanning at variable temperatures. A Pt/Ir tip is used for all the measurements. In our setup, the tip is grounded, while the voltage is applied to the sample. All the STM images shown in the following were acquired with the preamplifier gain setting of 10^8 V/A in the high speed mode [200 kHz cut-off frequency (-3 dB) and input noise of $130 \text{ fA}/\sqrt{\text{Hz}}$].

A. Conventional STM imaging

Au(111) was chosen as the first system for test. As shown in Fig. 11(a), the herringbone structure of the Au (111) has been clearly resolved after cleaning the sample by repeated cycles of Ar^+ bombardment at 1 kV and annealing to 800 K. To further verify the stability of our STM, we performed measurements on more complex systems. A silica bilayer film was grown on the Ru(0001) surface by evaporation of silicon on an O precovered substrate in 2×10^{-6} mbar O_2 for 15 min and subsequent annealing to 1200 K.⁶⁰ As shown in the zoomed-in STM image in Fig. 11(b), single O atoms are clearly imaged, which discloses the complex atomic arrangements in the silica film. There, a few six-membered rings form a small crystalline area incorporated in the amorphous film, which is an ideal system to study the interconversion between vitreous and crystalline phases of a silica film.^{20,21,60–64} It is important to note that typically the atomic resolution of silica is achieved only at low temperature and low noise setting ($4.3 \text{ fA}/\sqrt{\text{Hz}}$) of the preamplifier.⁶⁰ In our measurement, individual O and Si atoms within the silica network can be imaged at room temperature with high noise ($130 \text{ fA}/\sqrt{\text{Hz}}$) preamplifier setting, which demonstrates the success of our design concept.

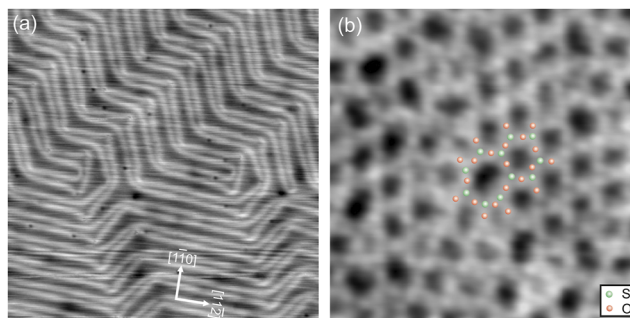


FIG. 11. Conventional STM images in a constant current mode at room temperature (300 K). (a) z image of the bare Au(111) surface with herringbone reconstruction, scan range $90 \times 90 \text{ nm}^2$, $I_T = 0.4 \text{ nA}$, $V_S = 0.6 \text{ V}$. Crystallographic orientations have been marked. (b) z image of the silica bilayer film on Ru(0001) with atomic resolution, scan range $5 \times 5 \text{ nm}^2$, $I_T = 0.5 \text{ nA}$, and $V_S = 1.6 \text{ V}$. O and Si positions are highlighted by the balls in red and green color, respectively. All the images shown here were acquired with the preamplifier gain setting of 10^8 V/A with an upper cut-off frequency (-3 dB) of 200 kHz.

STM imaging at elevated sample temperatures was also performed to demonstrate its function for variable temperature measurements. Terraces and steps of the Au(111) surface are shown in the overview STM image [Fig. 12(a)] acquired at a temperature of 400 K. Its herringbone reconstruction at high temperature is clearly resolved in both the overview and zoomed-in STM images [Fig. 12(b)]. With our presented instrument, STM images at sample temperatures of up to 500 K can be easily measured. Scanning at higher temperatures is possible with the sample clamped at the cryostat to more efficiently compensate the heating effect of the hot sample on the scanner.

As one step further, we measured surface dynamic processes with our instrument. Here, the diffusion of oxygen atoms on the Ru(0001) surface was chosen. A low-coverage oxygen layer was prepared on the clean Ru(0001) substrate by simply exposing the sample

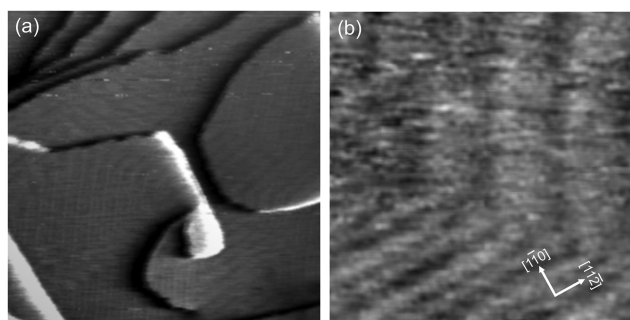


FIG. 12. Conventional STM images in a constant current mode at an elevated temperature (400 K). (a) Overview image of the tunneling current deviation of the Au(111) surface showing terraces and steps, scan range $120 \times 120 \text{ nm}^2$, $I_T = 1.0 \text{ nA}$, and $V_S = 1.0 \text{ V}$. (b) Zoomed-in STM image of the Au(111) surface showing the herringbone reconstruction, scan range $22 \times 22 \text{ nm}^2$, $I_T = 1.0 \text{ nA}$, and $V_S = 1.0 \text{ V}$. The crystallographic orientation of the reconstruction has been marked in (b). All the images shown here were acquired with the preamplifier gain setting of 10^8 V/A with an upper cut-off frequency (-3 dB) of 200 kHz.

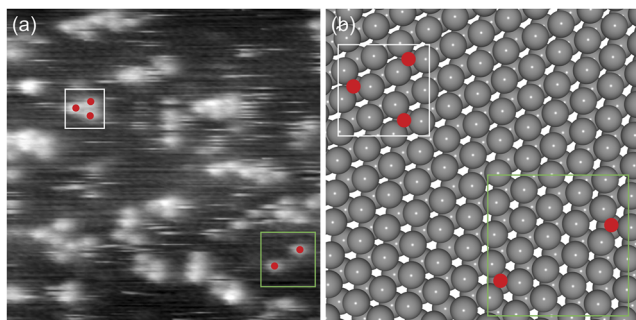


FIG. 13. Conventional constant current STM imaging of low-coverage oxygen atoms on Ru(0001) at room temperature (300 K). (a) High resolution STM image, scan range 9×9 nm, $I_T = 1.0$ nA, and $V_S = 1.0$ V. Isolated oxygen atoms and small clusters co-exist on the surface, as labeled by the red circles. The image was acquired with the preamplifier gain setting of 10^8 V/A with an upper cut-off frequency (-3 dB) of 200 kHz. (b) The adsorption model of oxygen atoms on Ru(0001): Ru atoms in gray and O atoms in red. Small clusters form (2×2) phase by occupying every two hcp sites (highlighted by the white square). Atoms separated by more than three surface-lattice constant are regarded as isolated (highlighted by the green square).

in 2×10^{-6} mbar O_2 for 30 s at room temperature. As shown in Fig. 13(a), the oxygen structures can be resolved by our STM with atomic resolution. Each protrusion corresponds to an oxygen atom, revealing the co-existence of isolated atoms and small clusters. Clusters exhibit the (2×2) structure with respect to the surface [Fig. 13(b)].^{2,65–67} Atoms separated by more than three surface-lattice constant are regarded as isolated.⁶⁸ The “dashes” in the STM image are attributed to diffusion of O atoms with a speed faster than the scanning speed in the x direction.¹⁵

B. High-speed STM imaging

In order to track the diffusion processes of oxygen atoms on the Ru(0001) surface, we performed high-speed STM imaging. Figure 14(a) shows the raw data of an STM image for the fast spiral scanning on a low-coverage oxygen adlayer. Individual oxygen atoms are resolved with an acquisition time of 33.3 ms per image. The images show higher resolution in the central area and slightly lower resolution at the edge of the image due to the uneven density of data points in the CAV scanning mode.⁴⁵ The atomic resolution is enhanced by applying a 2D Gaussian filter to the raw data [Fig. 14(b)]. To push the speed limit, scans with higher scan rates of 16.7 [Figs. 14(c) and 14(d)] and 8.3 ms [Figs. 14(e) and 14(f)] per image were performed. As shown in Fig. 14(e), atomic resolution is still preserved in the raw data when scanning with a rate of 120 frames per second. STM images from high-speed spiral scanning are used to generate videos for revealing the oxygen diffusion dynamics on Ru(0001). The video provided in the [supplementary material](#) is acquired with a scan speed of 16.7 ms per STM image. Within measurements of several minutes, which corresponds to thousands of frames, the videos show almost no drift of the scan position. Therefore, no drift correction was necessary. The images show little to no distortion effects and reveal the atomic lattice throughout the entire scan area.

Figures 15(a) and 15(b) present two continuous STM images taken from a video with a scan rate of 16.7 ms per image at room

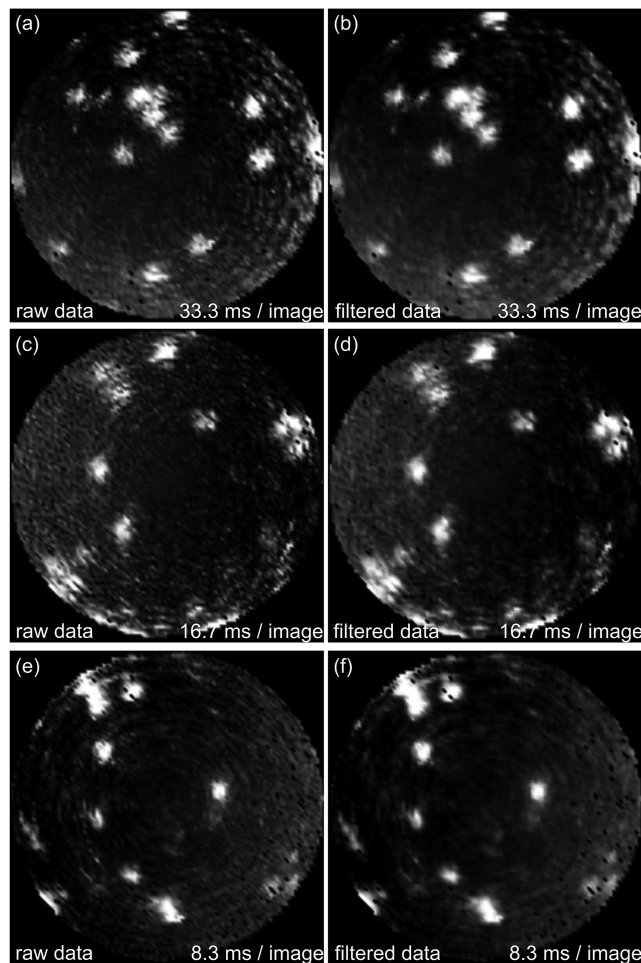


FIG. 14. High-speed STM images of the tunneling current deviation at room temperature (300 K) of a low-coverage oxygen structure with a scan speed of 33.3 ms (a) and (b), 16.7 ms (c) and (d), and 8.3 ms (e) and (f) per image, scan diameter = 5.0 nm, a slow feedback has been used for keeping an average I_T of 2.0 nA, $V_S = 0.9$ V. (a), (c), and (e) show the 2D histogram raw data (number of bins: 100). (b), (d), and (f) show the 2D histogram filtered data (2D Gaussian filter).

temperature (300 K). Since the diffusion rate of oxygen atoms is strongly influenced by inter-atom interactions, we only investigate the single atoms that are more than three surface lattice constant away from the nearest-neighboring oxygen atoms.⁶⁸ At room temperature, single oxygen atoms typically diffuse with a displacement of one surface lattice constant, as highlighted by the white square in Fig. 15(b). To inspect the influence of the temperature on the diffusion dynamics, we heat the sample to variable temperatures during STM scanning. Figures 15(c) and 15(d) show two continuous STM images with a scan rate of 16.7 ms per image at 330 K. There, a diffusion distance of two surface lattice constant is typically observed [white square in Fig. 15(d)]. A hopping rate of 7 s^{-1} is derived from the videos at 330 K, which is much faster than the diffusion at 300 K with a rate of 2 s^{-1} . The kinetic parameters for the diffusion processes of single oxygen atoms on Ru(0001) can be extracted from the

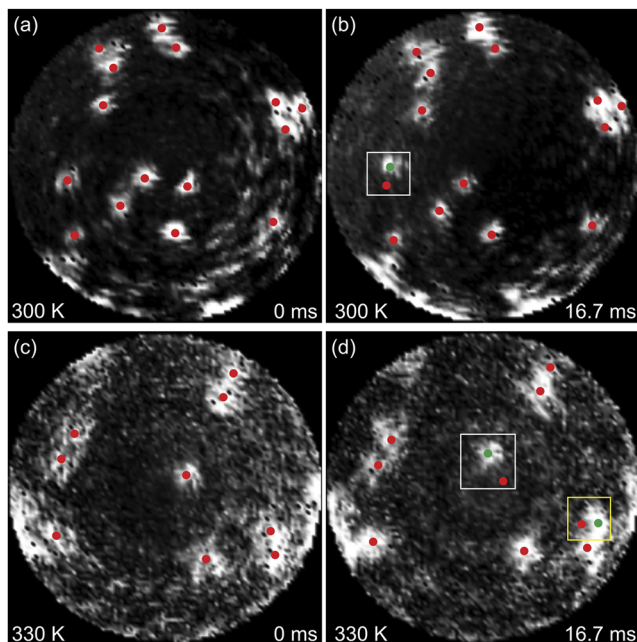


FIG. 15. High-speed STM images of the tunneling current deviation showing the diffusion of single oxygen atoms at different temperatures. (a) and (b) Two continuous STM images with a scan speed of 16.7 ms per image at 300 K, scan diameter = 5 nm, a slow feedback has been used for keeping an average I_T of 2.0 nA, $V_S = 0.9$ V. (c) and (d) Two continuous STM images with a scan speed of 16.7 ms per image at 330 K, scan diameter = 5 nm, a slow feedback has been used for keeping an average I_T of 2.0 nA, $V_S = 0.9$ V. The colored circles in the STM images indicate the position of oxygen atoms. The oxygen atoms in their initial positions have been marked by red dots, while green dots indicate the atoms that have been moved to a new position. The white squares highlight the diffusion of the single oxygen atoms (separated with neighbors by more than three surface-lattice constant). Typically, at 300 K, the single oxygen atom diffuses the distance of one surface lattice, while at 330 K, the diffusion distance is two surface lattices. The yellow square highlights the diffusion of an oxygen atom bonded with another one, which is not included in the statistics for the diffusion rate of single atoms.

variable temperature measurements and will be published in detail somewhere else.

IV. CONCLUSION AND OUTLOOK

We presented the design, construction, and first experimental results of a scanning tunneling microscope that operates with scan speeds above the video rate. The construction of a compact, rigid, and highly symmetric STM head ensures vibrational stability and low thermal drift. The design of a hybrid scanner composed of two independent tube piezos benefits tip positioning and feedback control during fast scanning. Spiral scanning geometry is used to avoid the limitations inherent to conventional raster scanning modes. Initial measurements show atomic resolution in both the conventional scanning and fast spiral scanning with a speed of 8.3 ms per image. The availability of preamplifiers and digitizers with wider bandwidth combined with improved spiral geometries would enable to push the scan speed beyond the millisecond range. Furthermore, *in situ* heating the sample to higher temperatures is demonstrated, which

enables future experiments, such as to resolve the interconversion between the crystalline and vitreous phases in glass films.^{20,21,60–64}

SUPPLEMENTARY MATERIAL

In the [supplementary material](#), we provide a video acquired with a scan speed of 16.7 ms per image. The video shows a 1 min sequence of spiral STM images of an oxygen covered Ru(0001) surface. The scan was performed at room temperature in quasi-constant height mode (scan diameter = 5 nm, $V_S = 0.9$ V, and a slow feedback has been used for keeping an average I_T of 2.0 nA). The frames show the fluctuation of the tunneling current and are reconstructed on a 100×100 grid by using 2D histograms as outlined in Sec. II E. The displayed real time is provided by the real time operating system (RTEMS) of the VMEbus system. The video is an example for the live video that can be monitored during the measurement, as mentioned in Sec. II E.

ACKNOWLEDGMENTS

The authors thank the mechanical workshop of the Fritz-Haber-Institut der Max-Planck-Gesellschaft for machining the chambers and the parts for the STM. The authors also thank the electronic workshop of the institute for producing some cables for the high-speed electronics. Furthermore, we would like to thank Wolf-Dieter Schneider for fruitful discussions. This project was financed by the European Research Council (ERC) under the European Union's Horizon 2020 Research and Innovation Program (Grant Agreement No. CRYVISIL-REP-669179). L.G. acknowledges support from the IMPRS EPPC.

AUTHOR DECLARATIONS

Conflict of Interest

The authors have no conflicts to disclose.

Author Contributions

Z.Y. and L.G. contributed equally to this work.

DATA AVAILABILITY

The data that support the findings of this study are available from the corresponding author upon reasonable request.

REFERENCES

- ¹G. Binnig, H. Rohrer, C. Gerber, and E. Weibel, "Surface studies by scanning tunneling microscopy," *Phys. Rev. Lett* **49**, 57–61 (1982).
- ²J. Wintterlin and R. Behm, in H.-J. Gtüntherodt and R. Wiesendanger (Eds.) *Scanning Tunneling Microscopy I* (Springer, 1994).
- ³(Eds.), *Scanning Probe Microscopy* (Springer, 2004).
- ⁴(Eds.), *Defects at Oxide Surfaces* (Springer, 2015).
- ⁵(Ed.), *Scanning Probe Microscopy* (Springer, 2015).
- ⁶A. H. Zewail, "Femtochemistry: Atomic-scale dynamics of the chemical bond using ultrafast lasers (Nobel Lecture)," *Angew. Chem., Int. Ed* **39**, 2586–2631 (2000).
- ⁷S. Loth, M. Etzkorn, C. P. Lutz, D. M. Eigler, and A. J. Heinrich, "Measurement of fast electron spin relaxation times with atomic resolution," *Science* **329**, 1628–1630 (2010).

- ⁸M. Morgenstern, "STM ready for the time domain," *Science* **329**, 1609–1610 (2010).
- ⁹Y. Terada, S. Yoshida, O. Takeuchi, and H. Shigekawa, "Real-space imaging of transient carrier dynamics by nanoscale pump-probe microscopy," *Nat. Photonics* **4**, 869 (2010).
- ¹⁰T. L. Cocker, V. Jelic, M. Gupta, S. J. Molesky, J. A. J. Burgess, G. De Los Reyes, L. V. Titova, Y. Y. Tsui, M. R. Freeman, and F. A. Hegmann, "An ultrafast terahertz scanning tunnelling microscope," *Nat. Photonics* **7**, 620 (2013).
- ¹¹T. L. Cocker, D. Peller, P. Yu, J. Repp, and R. Huber, "Tracking the ultrafast motion of a single molecule by femtosecond orbital imaging," *Nature* **539**, 263–267 (2016).
- ¹²B. C. Stipe, M. A. Rezaei, and W. Ho, "Single-molecule vibrational spectroscopy and microscopy," *Science* **280**, 1732–1735 (1998).
- ¹³J. Guo, J.-T. Lü, Y. Feng, J. Chen, J. Peng, Z. Lin, X. Meng, Z. Wang, X.-Z. Li, E.-G. Wang *et al.*, "Nuclear quantum effects of hydrogen bonds probed by tip-enhanced inelastic electron tunneling," *Science* **352**, 321–325 (2016).
- ¹⁴S. You, J.-T. Lü, J. Guo, and Y. Jiang, "Recent advances in inelastic electron tunneling spectroscopy," *Adv. Phys.: X* **2**, 907–936 (2017).
- ¹⁵J. Wintterlin, J. Trost, S. Renisch, R. Schuster, T. Zambelli, and G. Ertl, "Real-time STM observations of atomic equilibrium fluctuations in an adsorbate system: O/Ru(0001)," *Surf. Sci* **394**, 159–169 (1997).
- ¹⁶L. R. Merte, G. Peng, R. Bechstein, F. Rieboldt, C. A. Farberow, L. C. Grabow, W. Kudernatsch, S. Wendt, E. Lægsgaard, M. Mavrikakis, and F. Besenbacher, "Water-mediated proton hopping on an iron oxide surface," *Science* **336**, 889–893 (2012).
- ¹⁷G. Dong, E. B. Fourré, F. C. Tabak, and J. W. M. Frenken, "How boron nitride forms a regular nanomesh on Rh(111)," *Phys. Rev. Lett* **104**, 096102 (2010).
- ¹⁸G. C. Dong, D. W. van Baarle, M. J. Rost, and J. W. M. Frenken, "Graphene formation on metal surfaces investigated by in-situ scanning tunneling microscopy," *New J. Phys* **14**, 053033 (2012).
- ¹⁹L. L. Patera, F. Bianchini, C. Africh, C. Dri, G. Soldano, M. M. Mariscal, M. Peressi, and G. Comelli, "Real-time imaging of adatom-promoted graphene growth on nickel," *Science* **359**, 1243–1246 (2018).
- ²⁰P. Y. Huang, S. Kurasch, J. S. Alden, A. Shekhawat, A. A. Alemi, P. L. McEuen, J. P. Sethna, U. Kaiser, and D. A. Muller, "Imaging atomic rearrangements in two-dimensional silica glass: Watching silica's dance," *Science* **342**, 224–227 (2013).
- ²¹H.-J. Freund, "Controlling silica in its crystalline and amorphous states: A problem in surface science," *Acc. Chem. Res* **50**, 446–449 (2017).
- ²²J. Wintterlin, S. Völkening, T. V. W. Janssens, T. Zambelli, and G. Ertl, "Atomic and macroscopic reaction rates of a surface-catalyzed reaction," *Science* **278**, 1931–1934 (1997).
- ²³C. Sachs, M. Hildebrand, S. Völkening, J. Wintterlin, and G. Ertl, "Reaction fronts in the oxidation of hydrogen on Pt(111): Scanning tunneling microscopy experiments and reaction-diffusion modeling," *J. Chem. Phys* **116**, 5759–5773 (2002).
- ²⁴O. M. Magnussen, "Atomic-scale insights into electrode surface dynamics by high-speed scanning probe microscopy," *Chem. - Eur. J* **25**, 12865–12883 (2019).
- ²⁵Q. Li and Q. Lu, "Atomic resolution ultrafast scanning tunneling microscope with scan rate breaking the resonant frequency of a quartz tuning fork resonator," *Rev. Sci. Instrum* **82**, 053705 (2011).
- ²⁶C. Dri, M. Panighel, D. Tiemann, L. L. Patera, G. Troiano, Y. Fukamori, F. Knoller, B. A. J. Lechner, G. Cautero, D. Giuressi, G. Comelli, J. Fraxedas, C. Africh, and F. Esch, "The new FAST module: A portable and transparent add-on module for time-resolved investigations with commercial scanning probe microscopes," *Ultramicroscopy* **205**, 49–56 (2019).
- ²⁷M. J. Rost, L. Crama, P. Schakel, E. van Tol, G. B. E. M. van Velzen-Williams, C. F. Overgaw, H. ter Horst, H. Dekker, B. Okhuijsen, M. Seynen, A. Vijftigschild, P. Han, A. J. Katan, K. Schoots, R. Schumm, W. van Loo, T. H. Oosterkamp, and J. W. M. Frenken, "Scanning probe microscopes go video rate and beyond," *Rev. Sci. Instrum* **76**, 053710 (2005).
- ²⁸F. Esch, C. Dri, A. Spessot, C. Africh, G. Cautero, D. Giuressi, R. Sergio, R. Tommasini, and G. Comelli, "The FAST module: An add-on unit for driving commercial scanning probe microscopes at video rate and beyond," *Rev. Sci. Instrum* **82**, 053702 (2011).
- ²⁹L. Kuipers, R. W. M. Loos, H. Neerings, J. ter Horst, G. J. Ruwiel, A. P. de Jongh, and J. W. M. Frenken, "Design and performance of a high-temperature, high-speed scanning tunneling microscope," *Rev. Sci. Instrum* **66**, 4557–4565 (1995).
- ³⁰S. H. Pan, E. W. Hudson, and J. C. Davis, "³He refrigerator based very low temperature scanning tunneling microscope," *Rev. Sci. Instrum* **70**, 1459–1463 (1999).
- ³¹C. Y. Nakakura, V. M. Phanse, G. Zheng, G. Bannon, E. I. Altman, and K. P. Lee, "A high-speed variable-temperature ultrahigh vacuum scanning tunneling microscope," *Rev. Sci. Instrum* **69**, 3251–3258 (1998).
- ³²L. Petersen, M. Schunack, B. Schaefer, T. R. Linderoth, P. B. Rasmussen, P. T. Sprunger, E. Laegsgaard, I. Stensgaard, and F. Besenbacher, "A fast-scanning, low- and variable-temperature scanning tunneling microscope," *Rev. Sci. Instrum* **72**, 1438–1444 (2001).
- ³³G. Schitter and M. J. Rost, "Scanning probe microscopy at video-rate," *Mater. Today* **11**, 40–48 (2008).
- ³⁴M. J. Rost, G. J. C. van Baarle, A. J. Katan, W. M. van Spengen, P. Schakel, W. A. van Loo, T. H. Oosterkamp, and J. W. M. Frenken, "Video-rate scanning probe control challenges: Setting the stage for a microscopy revolution," *Asian J. Control* **11**, 110–129 (2009).
- ³⁵J. W. Frenken and I. M. Groot, "Seeing dynamic phenomena with live scanning tunneling microscopy," *MRS Bull* **42**, 834–841 (2017).
- ³⁶Y.-C. Yang, A. Taranovskyy, and O. M. Magnussen, "Thiolate-induced metal adatom trapping at solid-liquid interfaces," *Angew. Chem., Int. Ed. Engl* **51**, 1966–1969 (2012).
- ³⁷Q. F. Li, Y. Wang, F. Wang, Y. Hou, and Q. Lu, "100 MHz large bandwidth preamplifier and record-breaking 50 kHz scanning rate quantum point contact mode probe microscopy imaging with atomic resolution," *Rev. Sci. Instrum* **92**, 013701 (2021).
- ³⁸A.-K. Hens, J. Wiechers, R. Schuster, V. Platschkowski, and J. Wintterlin, "A beetle-type, variable-temperature scanning tunneling microscope for video-rate imaging," *Jpn. J. Appl. Phys* **59**, SN1007 (2020).
- ³⁹T. Tuma, J. Lygeros, V. Kartik, A. Sebastian, and A. Pantazi, "High-speed multiresolution scanning probe microscopy based on Lissajous scan trajectories," *Nanotechnology* **23**, 185501 (2012).
- ⁴⁰D. Ziegler, T. R. Meyer, R. Farnham, C. Brune, A. L. Bertozzi, and P. D. Ashby, "Improved accuracy and speed in scanning probe microscopy by image reconstruction from non-gridded position sensor data," *Nanotechnology* **24**, 335703 (2013).
- ⁴¹Y. R. Teo, Y. K. Yong, and A. J. Fleming, "A review of scanning methods and control implications for scanning probe microscopy," in *2016 American Control Conference (ACC)* (IEEE, 2016), pp. 7377–7383.
- ⁴²X. Sang, A. R. Lupini, R. R. Unocic, M. Chi, A. Y. Borisevich, S. V. Kalinin, E. Endeve, R. K. Archibald, and S. Jesse, "Dynamic scan control in STEM: Spiral scans," *Adv. Struct. Chem. Imaging* **2**, 6 (2016).
- ⁴³Y. R. Teo, Y. Yong, and A. J. Fleming, "A comparison of scanning methods and the vertical control implications for scanning probe microscopy," *Asian J. Control* **20**, 1352–1366 (2018).
- ⁴⁴D. Momotenko, J. C. Byers, K. McKelvey, M. Kang, and P. R. Unwin, "High-speed electrochemical imaging," *ACS Nano* **9**, 8942–8952 (2015).
- ⁴⁵D. Ziegler, T. R. Meyer, A. Amrein, A. L. Bertozzi, and P. D. Ashby, "Ideal scan path for high-speed atomic force microscopy," *IEEE/ASME Trans. Mechatron* **22**, 381–391 (2017).
- ⁴⁶J. Wang, J. Wang, Y. Hou, and Q. Lu, "Self-manifestation and universal correction of image distortion in scanning tunneling microscopy with spiral scan," *Rev. Sci. Instrum* **81**, 073705 (2010).
- ⁴⁷Q. Wang, Y. Hou, J. Wang, and Q. Lu, "A high-stability scanning tunneling microscope achieved by an isolated tiny scanner with low voltage imaging capability," *Rev. Sci. Instrum* **84**, 113703 (2013).
- ⁴⁸See <https://www.specs-group.com/nanonis/products/mimea/> for Nanonis SPM control system.
- ⁴⁹See <https://leidenprobemicroscopy.com/support-equipment/> for Leiden preamplifier.
- ⁵⁰See <https://www.struck.de/sis1350.html> for SIS1350 digitizer.
- ⁵¹See <https://www.falco-systems.com/products.html> for high speed high voltage amplifier WMA-300.

- ⁵²M. S. Hoogeman, D. G. van Loon, R. W. M. Loos, H. G. Ficke, E. de Haas, J. J. van der Linden, H. Zeijlemaker, L. Kuipers, M. F. Chang, M. A. J. Klik, and J. W. M. Frenken, "Design and performance of a programmable-temperature scanning tunneling microscope," *Rev. Sci. Instrum.* **69**, 2072–2080 (1998).
- ⁵³V. Navarro, M. A. van Spronsen, and J. W. M. Frenken, "In situ observation of self-assembled hydrocarbon Fischer–Tropsch products on a cobalt catalyst," *Nat. Chem.* **8**, 929 (2016).
- ⁵⁴H. Hibino, T. Fukuda, M. Suzuki, Y. Homma, T. Sato, M. Iwatsuki, K. Miki, and H. Tokumoto, "High-temperature scanning-tunneling-microscopy observation of phase transitions and reconstruction on a vicinal Si(111) surface," *Phys. Rev. B* **47**, 13027 (1993).
- ⁵⁵B. C. Stipe, M. A. Rezaei, and W. Ho, "A variable-temperature scanning tunneling microscope capable of single-molecule vibrational spectroscopy," *Rev. Sci. Instrum.* **70**, 137–143 (1999).
- ⁵⁶H. Junkes, H.-J. Freund, L. Gura, M. Heyde, P. Marschalik, and Z. Yang, "Experiment control with EPICS7 and symmetric multiprocessing on RTEMs," in *Proceedings of the International Conference on Accelerator and Large Experimental Control Systems (ICALEPCS'17)*, Geneva, Switzerland, 2018, <http://www.jacow.org>, Vol. 16, pp. 1762–1766.
- ⁵⁷L. Gura, Z. Yang, M. Brinker, F. Kalaß, W. Kirstaedter, P. Marschalik, H. Junkes, M. Heyde, and H.-J. Freund, "Spiral high-speed scanning tunneling microscopy: Tracking atomic diffusion on the millisecond timescale," *Appl. Phys. Lett.* **119**, 251601 (2021).
- ⁵⁸L. Gura and M. Brinker, Point Cloud Visualization and Analysis, GitHub repository, https://github.com/molgen.mpg.de/gura/point_cloud_visualization_and_analysis, 2021.
- ⁵⁹S. Veseli, "PvaPy: Python API for EPICS PV access," in *Proceedings of ICALEPCS2015*, Melbourne, Australia, (JACoW Publishing, 2015).
- ⁶⁰L. Lichtenstein, C. Büchner, B. Yang, S. Shaikhutdinov, M. Heyde, M. Sierka, R. Włodarczyk, J. Sauer, and H.-J. Freund, "The atomic structure of a metal-supported vitreous thin silica film," *Angew. Chem., Int. Ed.* **51**, 404–407 (2012).
- ⁶¹D. Löffler, J. J. Uhlrich, M. Baron, B. Yang, X. Yu, L. Lichtenstein, L. Heinke, C. Büchner, M. Heyde, S. Shaikhutdinov, H.-J. Freund, R. Włodarczyk, M. Sierka, and J. Sauer, "Growth and structure of crystalline silica sheet on Ru(0001)," *Phys. Rev. Lett.* **105**, 146104 (2010).
- ⁶²L. Lichtenstein, M. Heyde, and H.-J. Freund, "Crystalline-vitreous interface in two dimensional silica," *Phys. Rev. Lett.* **109**, 106101 (2012).
- ⁶³P. Y. Huang, S. Kurasch, A. Srivastava, V. Skakalova, J. Kotakoski, A. V. Krashennikov, R. Hovden, Q. Mao, J. C. Meyer, J. Smet, D. A. Muller, and U. Kaiser, "Direct imaging of a two-dimensional silica glass on graphene," *Nano Lett.* **12**, 1081–1086 (2012).
- ⁶⁴H. W. Klemm, M. J. Prieto, F. Xiong, G. B. Hassine, M. Heyde, D. Menzel, M. Sierka, T. Schmidt, and H.-J. Freund, "Silica bilayer supported on Ru(0001): Following the crystalline to vitreous transformation in real time with spectro-microscopy," *Angew. Chem., Int. Ed.* **59**, 10587 (2020).
- ⁶⁵K. Meinel, H. Wolter, C. Ammer, A. Beckmann, and H. Neddermeyer, "Adsorption stages of O on Ru(0001) studied by means of scanning tunneling microscopy," *J. Phys.: Condens. Matter* **9**, 4611–4619 (1997).
- ⁶⁶F. Calleja, A. Arnau, J. J. Hinarejos, A. L. Vázquez de Parga, W. A. Hofer, P. M. Echenique, and R. Miranda, "Contrast reversal and shape changes of atomic adsorbates measured with scanning tunneling microscopy," *Phys. Rev. Lett.* **92**, 206101 (2004).
- ⁶⁷H. Over, "Surface chemistry of ruthenium dioxide in heterogeneous catalysis and electrocatalysis: From fundamental to applied research," *Chem. Rev.* **112**, 3356–3426 (2012).
- ⁶⁸S. Renisch, R. Schuster, J. Wintterlin, and G. Ertl, "Dynamics of adatom motion under the influence of mutual interactions: O/Ru(0001)," *Phys. Rev. Lett.* **82**, 3839–3842 (1999).